ISSN 1990-7931, Russian Journal of Physical Chemistry B, 2025, Vol. 19, No. 1, pp. 217–235. © Pleiades Publishing, Ltd., 2025.

CHEMICAL PHYSICS OF NANOMATERIALS

Modelling and Characterization of Silicon and Germanium Oxides as Nano-Hybrid Materials for Hydrogen Storage in Cell Batteries: a First-Principle Study

F. Mollaamin[a, *], M. Monajjemi[b], S. Mohammadi[b], and S. Shahriari[c]

[a] *Department of Biomedical Engineering, Faculty of Engineering and Architecture, Kastamonu University, Kastamonu, Turkey*

[b] *Department of Chemical Engineering, Central Tehran Branch, Islamic Azad University, Tehran, Iran*

[c] *Department of Chemistry, Central Tehran Branch, Islamic Azad University, Tehran, Iran*

**e-mail: fmollaamin@kastamonu.edu.tr*

Received June 20, 2024; revised August 2, 2024; accepted August 20, 2024

Abstract—As applied materials for energy storage, Si_5O_{10}–Ge_5O_{10} can attract considerable attention in materials science. A comprehensive investigation on hydrogen grabbing by Si_5O_{10}–Ge_5O_{10} was carried out including using density functional theory computations at the CAM–B3LYP–D3/6-311+G(d, p) level of theory. The data represents that if silicon elements are replaced by germanium, the H-grabbing energy will be ameliorated. Electromagnetic and thermodynamic properties of Si_5O_{10}, Ge_5O_{10} and Si_5O_{10}–Ge_5O_{10} nanoclusters have been evaluated. The hypothesis of the hydrogen adsorption phenomenon was confirmed by density distributions of charge density differences, total density of states and electron localization function for hydrated nanoclusters of H–Si_5O_{10}, H–Ge_5O_{10} and H–Si_5O_{10}–Ge_5O_{10}–H. The fluctuation in charge density values demonstrates that the electronic densities were mainly located in the boundary of adsorbate/adsorbent atoms during the adsorption status. As the advantages of germanium over silicon include its higher electron and hole mobility, allowing germanium devices to operate at higher frequencies than silicon devices. Therefore, by combination of Si_5O_{10} and Ge_5O_{10}, it can be concluded that Si_5O_{10}–Ge_5O_{10} nanocluster might be appropriate candidate for hydrogen storage in cell batteries.

Keywords: Si_5O_{10}–Ge_5O_{10}, hydrogen storage, nanomaterial, DFT

DOI: 10.1134/S1990793124701677

1. INTRODUCTION

A type of clean fuel is hydrogen that might be employed to accumulate, carry, and spread energy produced by other sources and it generates water when applied in a fuel cell [1]. A fuel cell applies reverse electrolysis to convert an oxidizing agent and hydrogen to power an electric motor [2–4]. CNTs owing to their lightness, tube construction, vast plane and high reactivity between C and H atoms can be proposed as a promising material for H-grabbing [5–8].

It was investigated that H-storing on C-nano compound indicates the molecular hydrogen dissociation [9–12]. The structure of transition metal-carbon exhibits a charge distribution among boundary atoms and the cationic state of transition metals can be discussed [13–17]. Thus, the electronic charge can be produced through gas molecules adsorption on the surfaces of ionic transition metal [18–20]. Transition metals as dopants might make a whole Hamiltonian perturbation towards alterations in electronic structures, which convert it a substantial usage in magnetic electronic instruments [21–25]. Recently, Si-, Ge- or Sn-carbide nanostructures have been suggested as engaged H-grabbing compounds [26–28]. Since the polarizability of silicon is more than carbon, it is supposed that Si–C/Si nanosheet might attach to compositions more strongly in comparison to the net carbon nano-surfaces [29–31].

H_2 gas is mostly preserved either by liquefaction under high compressing pressure [32–35] or by adsorption on the surface or interstitial region of material cavity [36–38]. In relation to this, the adsorption of H_2 on the surface of 2D materials has advantages in terms of safe functionality and cost-effectiveness. For the effective utilization of H_2 in fuel cells, the adsorption energy and gravimetric weight percentage on the adsorbent should be sufficiently high [39]. The adsorption-desorption kinetics and the strength of binding energy ought to be intermediate for hydrogen to bind on the material surfaces with an optimal adsorption energy range.

Moreover, the adsorption and sensing of H_2 and CH_2O molecules on the pristine and transition metal consisting of V, Cr, Mn, Nb, Mo, Tc, Ta, W, or Re

doping on B or N site of boron nitride nanosheets. The achieved results exhibit that the pristine BNNS indicates fragile interaction with the H_2 and CH_2O molecules. The H_2 and CH_2O molecules might be strongly adsorption on the transition metal doped BNNSs with appreciable adsorption energy through the geometrical deformation on the transition metal doping zone [40].

In our previous works, the investigation of energy storage in fuel cells through hydrogen adsorption has been accomplished using DFT calculations through different nanomaterials consisting of silicon/germanium/tin/lead nano-carbides [41], magnesium -aluminum alloy [42] and aluminum/carbon/ silicon doping boron nitride nanocage [43]. Nanomaterials with remarkable specific structures indicate promising applications in the field of energy storage, electrocatalysis, and fuel cells.

The researchers have reported theoretical investigation of guanine adsorption on some small clusters including SiO_2, Si_2O_4, Si_3O_6, Si_4O_8 and Si_5O_{10} in terms of geometry, binding energy, binding site, energy gap, electronic and spectral properties. Moreover, experimental results are compared with the DFT results. Further the sol-gel silicate material used to protect the DNA base from UVA- irradiation has been highlighted [44].

Two novel porous germanates, $[Ge_5O_{10}](H_2O)$ and $[Ge_{10}O_{20}OH][(CH_3)_4N]$, were synthesized by a hydrothermal method using TMA (tetramethylammonium), and characterized by X-ray crystallography, indicating that a new sample of three membered rings including two octahedral GeO_6 and one tetrahedral GeO_4 is in $[Ge_5O_{10}](H_2O)$, and the OH^- anions are placed in the center of double 4-membered rings in $[Ge_{10}O_{20}OH][(CH_3)_4N]$ [45]. A new germanate $[Ge_9O_{14}(OH)_{12}](C_6N_2H_{16})_2{\cdot}H_2O$ was synthesized under hydrothermal conditions and its structure characterized by X-ray crystallography. This structure contains Ge–O layers of helical chains, which are linked by hydrogen bonds to form a soft, open framework that indicates a selectivity for *cis*-1,4-diaminocyclohexane during the synthesis [46].

Therefore, this work wants to demonstrate a facile approach for fabricating nanocluster of Si_5O_{10}–Ge_5O_{10} as a template at a moderate condition for hydrogen storage. In the field of semiconductor materials, germanium and silicon are essential components that have greatly influenced modern technology. They are vital in electronics, each with its own distinct properties that make them valuable for different purposes. This article examines the basic difference between germanium and silicon through two complexes of Si_5O_{10}, Ge_5O_{10}, and formation of Si_5O_{10}–Ge_5O_{10} nanocluster including their electrical characteristics and practical uses in different technological fields. One of its notable uses is in the semiconductor industry. Germanium was initially used in early cell batteries and semiconductors, playing a crucial role in the development of electronic devices. However, silicon largely replaced germanium. Despite this, germanium is still used in some niche applications, such as infrared detectors and optical devices. Currently, the present research aims to explore the possibility of using Si_5O_{10}–Ge_5O_{10} nanocluster for hydrogen storage by employing first-principles calculations. We have analyzed the structural and electronic properties of Si_5O_{10}, Ge_5O_{10}, Si_5O_{10}–Ge_5O_{10} and hydrated nanocluster of H–Si_5O_{10}–Ge_5O_{10}–H using state-of-the-art computational techniques.

2. THEORY, MATERIALS AND COMPUTATION

The aim of this study is to hydrogen adsorption by using Si_5O_{10}, Ge_5O_{10}, Si_5O_{10}–Ge_5O_{10} nanoclusters (Fig. 1). Hydrated nanocluster of H–Si_5O_{10}–Ge_5O_{10}–H was modeled in the presence of Si_5O_{10}, Ge_5O_{10} and production of Si_5O_{10}–Ge_5O_{10} which can increase the hydrogen storage in cell batteries. Whether in gas approximation or in solvation simulation, the density functional theory with London dispersion correction (DFT–D3) demonstrates that combination of Si_5O_{10} and Ge_5O_{10} and producing Si_5O_{10}–Ge_5O_{10} nanocluster can stably exist for hydrogen storage in the cell batteries through formation of H–Si_5O_{10}–Ge_5O_{10}–H at CAM–B3LYP–D3 [47]. Therefore, the calculations have been done by CAM–B3LYP–D3/EPR-3 level of theory.

Figure 1 has shown the process of hydrogen adsorption on Si_5O_{10}–Ge_5O_{10} surface which includes the formation of hydrated nanoclusters containing H–Si_5O_{10}, H–Ge_5O_{10}, H–Si_5O_{10}–Ge_5O_{10}–H. The Bader charge analysis [48] was discussed during trapping of hydrogen atoms by Si_5O_{10}–Ge_5O_{10} and formation of H–Si_5O_{10}, H–Ge_5O_{10}, H–Si_5O_{10}–Ge_5O_{10}–H nanoclusters (Fig. 1). The rigid potential energy surface using density functional theory [49–62] was performed due to Gaussian 16 revision C.01 program package [63] and GaussView 6.1 [64]. The coordination input for hydrogen grabbing by Si_5O_{10}–Ge_5O_{10} has applied 6-311+G(d, p) and EPR-3 basis sets.

3. RESULTS AND DISCUSSION

3.1. Charge Density Differences, Total Density of States and Electron Localization Function Analysis

The amounts of charge density differences (CDD) are measured by considering isolated atoms or noninteracting ones. The mentioned approximation can be the lightest to use because the superposition value may be received from the primary status of the self-consistency cycle in the code that carries out the density functional theory (Fig. 2) [65]. In Fig. 2a, the atoms of O2, O3, O7, O8, O12, O14, O15 from Si_5O_{10} have shown the fluctuation around –9 to –3 Bohr towards formation of H–Si_5O_{10} (Fig. 2b). And, the atoms of O3, O7, O8, O12, O14, O15 in Ge_5O_{10} (Fig. 2c) have

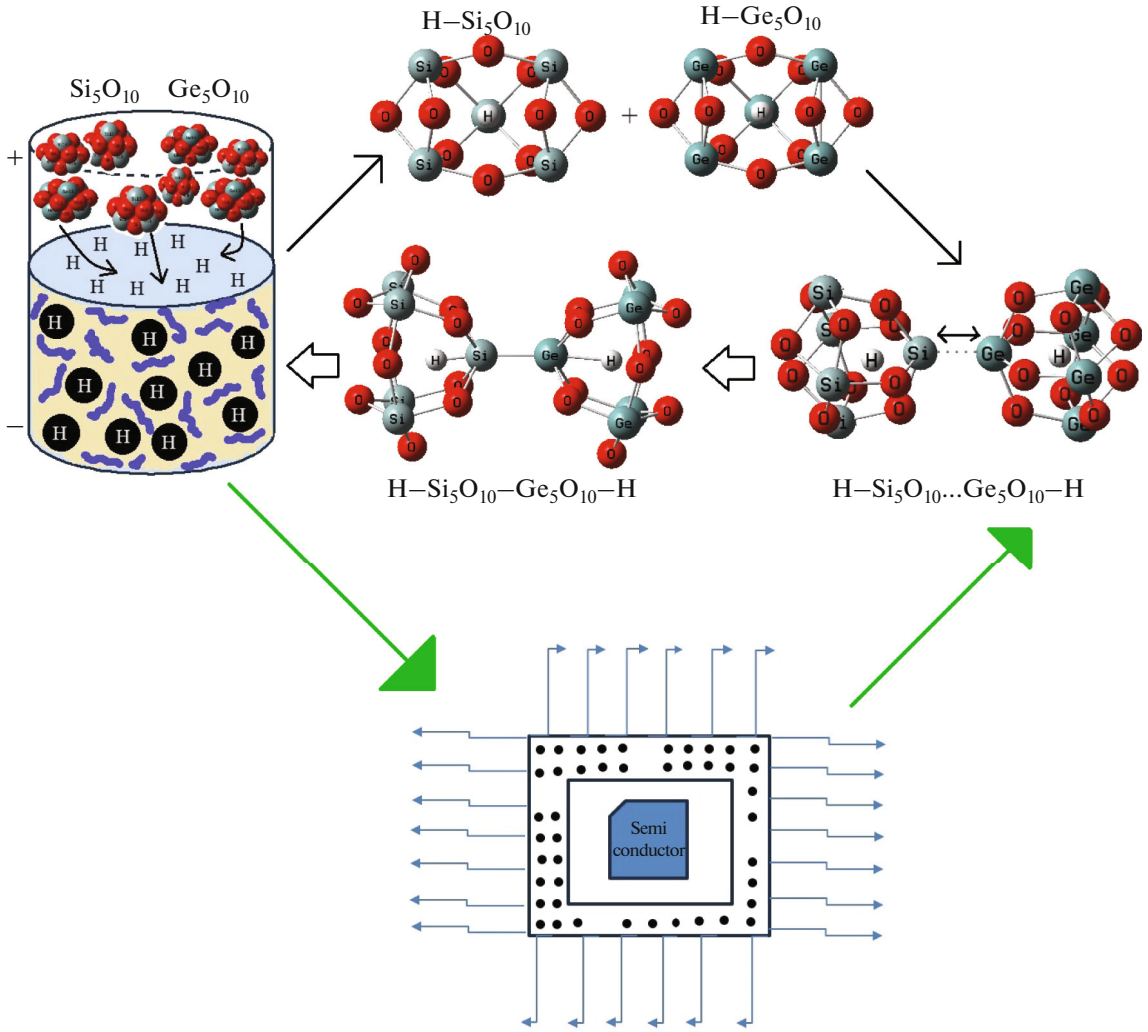

Fig. 1. Application of Si_5O_{10}–Ge_5O_{10} for increasing hydrogen adsorption towards the energy storage in cell batteries accompanying formation of hydrated nanoclusters including H–Si_5O_{10}, H–Ge_5O_{10}, H–Si_5O_{10}–Ge_5O_{10}–H using CAM–B3LYP–D3/6-311+G(d, p) calculation.

indicated the fluctuation around –9 to +2 Bohr towards formation of H–Ge_5O_{10} (Fig. 2d). Furthermore, Si_5O_{10}–Ge_5O_{10} (Fig. 2e) cluster with the fluctuation in the region around –12 to +6 Bohr becomes towards formation of H–Si_5O_{10}–Ge_5O_{10}–H hydrated cluster (Fig. 2f) in the area around –12 to +10 Bohr.

Squirming the molecular orbital data owing to gaussian graphs of unit altitude and entire width at half maximum (FWHM) of 0.3 eV by GaussSum 3.0.2 [66] have computed total density of states (TDOS) diagrams. To better understand the adsorption characteristics of hydrogen by crystals of Si_5O_{10}, Ge_5O_{10}, and Si_5O_{10}–Ge_5O_{10} cluster, TDOS has been measured. This parameter can indicate the existence of important chemical interactions often on the convex side (Fig. 3). The maximum energy of TDOS for Si_5O_{10} (Fig. 3a) and Ge_5O_{10} (Fig. 3b) with three sharp peaks around –0.35, –0.45 and –0.65 a.u. with maximum density of state of 10 around –0.35 a.u. has been shown. Moreover, the similar amounts of TDOS for complexes of H–Si_5O_{10} (Fig. 3a') and H–Si_5O_{10}, (Fig. 3b') through some fluctuations in the behavior of the graphs have been observed. During formation of Si_5O_{10}–Ge_5O_{10} cluster, Fig. 3c has shown sharp and sophisticated peaks around –0.3, –0.45 and –0.65 a.u. due to covalent bond between two crystals of Si_5O_{10} and Ge_5O_{10}. However, after H-grabbing by Si_5O_{10}–Ge_5O_{10} cluster, Fig. 3c' has represented sharp and sophisticated peaks for the hydrated cluster of H–Si_5O_{10}–Ge_5O_{10}–H around –0.32, –0.45 and a sharper peak than Si_5O_{10}–Ge_5O_{10} around –0.6 a.u. due to hydrogen adsorption and covalent bond between two crystals of Si_5O_{10} and Ge_5O_{10}.

Furthermore, a type of scalar fields called electron localization function (ELF) may demonstrate a broad span of bonding samples. Nevertheless, the distinction

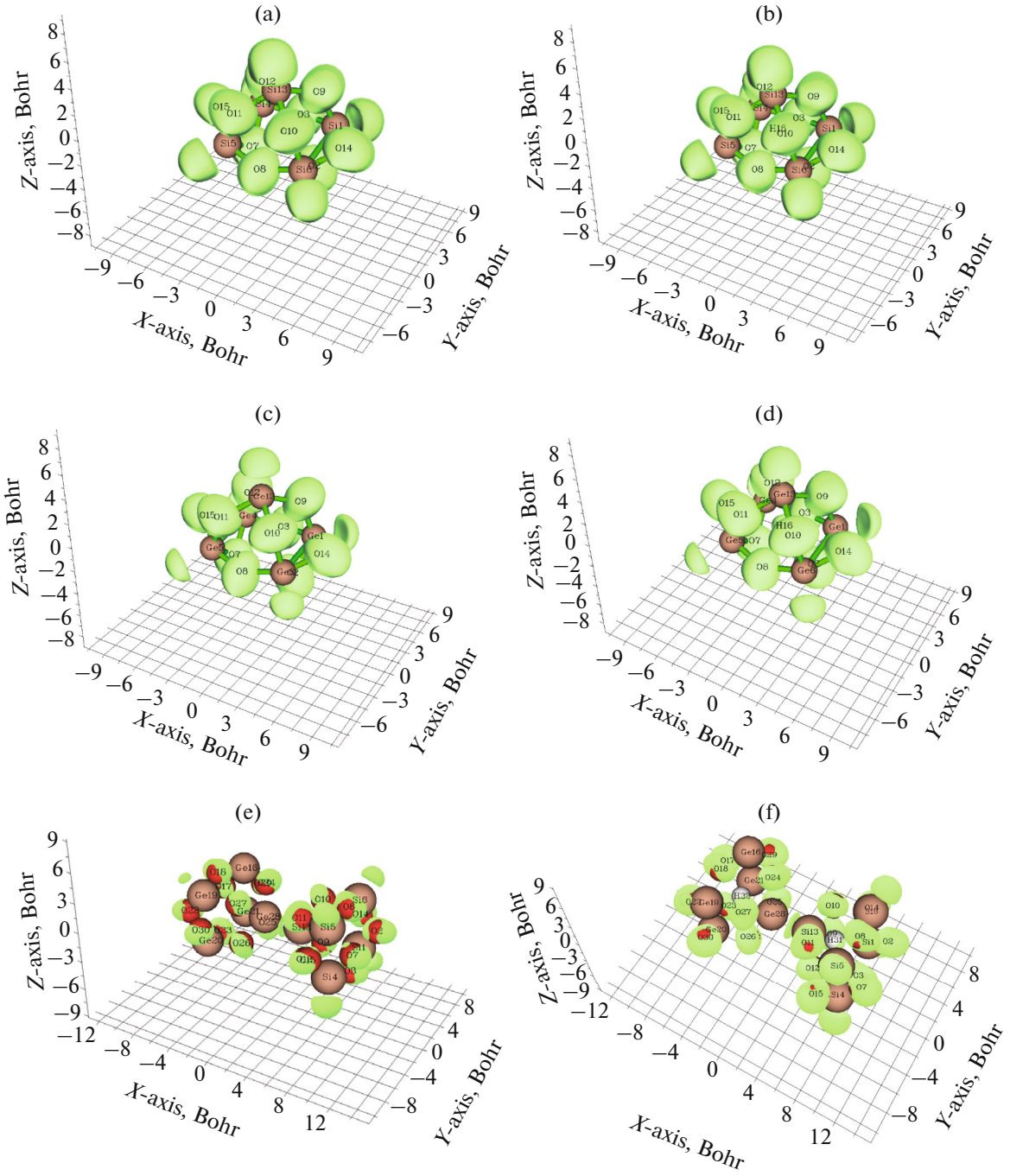

Fig. 2. CDD graphs for (a) Si_5O_{10}, (b) H–Si_5O_{10}, (c) Ge_5O_{10}, (d) H–Ge_5O_{10}, (e) Si_5O_{10}–Ge_5O_{10} and (f) H–Si_5O_{10}–Ge_5O_{10}–H.

between deduced/raised electron delocalization/localization into cyclic π-conjugated sets stays encouraging for ELF [67]. The grosser the electron localization is in an area, the more likely the electron movement is restricted within it. Therefore, they might be discerned from the ones away if electrons are totally centralized. As Bader investigated, the zones with large electron localization possess extensive magnitudes of Fermi hole integration [68]. But, with having a six-dimension function for the Fermi hole, it seems hard to be studied directly. Then, Becke and Edgecombe remarked that spherically averaged like spin conditional pair probability possesses a direct correlation with the Fermi hole and proposed the parameter of ELF in Multiwfn program [69] and popularized for spin-polarized procedure [70]:

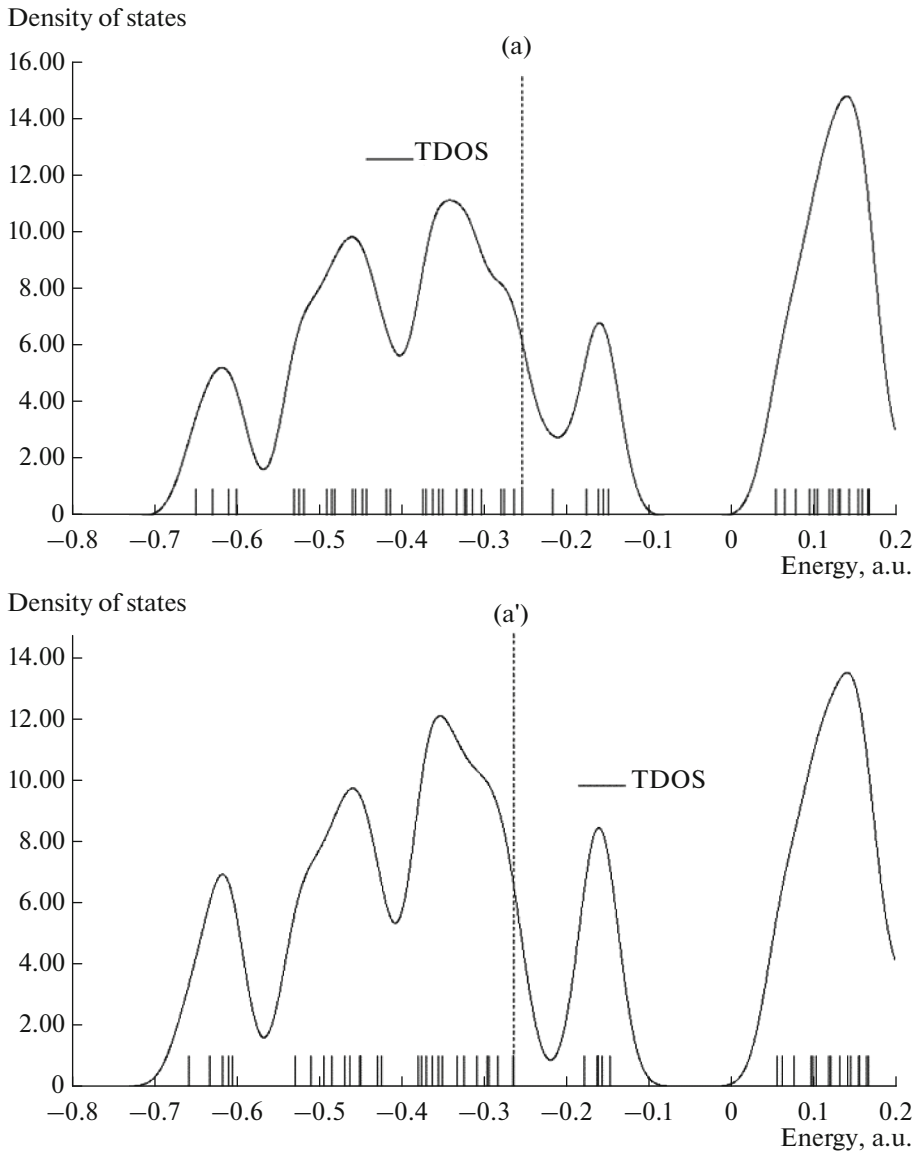

Fig. 3. TDOS graphs of (a) Si_5O_{10}, (a') H–Si_5O_{10}, (b) Ge_5O_{10}, (b') H–Ge_5O_{10}, (c) Si_5O_{10}–Ge_5O_{10} and (c') H–Si_5O_{10}–Ge_5O_{10}–H.

$$\mathrm{ELF}(r) = \frac{1}{1 + [D(r)/D_0(r)]}, \quad (1)$$

where

$$D(r) = \frac{1}{2}\sum_i \eta_i |\nabla\varphi_i(r)|^2 - \frac{1}{8}\left[\frac{|\nabla\rho_\alpha(r)|^2}{\rho_\alpha(r)} + \frac{|\nabla\rho_\beta(r)|^2}{\rho_\beta(r)}\right], \quad (2)$$

and

$$D_0(r) = \frac{3}{10}\left(6\pi^2\right)^{2/3}\left[\rho_\alpha(r)^{5/3} + \rho_\beta(r)^{5/3}\right]. \quad (3)$$

For close-shell system, since $\rho_\alpha = \rho_\beta = (1/2)\rho$, D and D_0 terms can be simplified as:

$$D(r) = \frac{1}{2}\sum_i \eta_i |\nabla\varphi_i(r)|^2 - \frac{1}{8}\frac{|\nabla\rho(r)|^2}{\rho(r)}, \quad (4)$$

and

$$D_0(r) = (3/10)\left(3\pi^2\right)^{2/3}\rho(r)^{5/3}. \quad (5)$$

Regarding kinetic energy, ELF was rechecked to be more punctual for both Kohn–Sham DFT and post-HF wavefunctions [71]. In fact, the excess kinetic energy density caused by Pauli repulsion was unfolded by $D(r)$ and $D_0(r)$ may be inspected as Thomas–Fermi kinetic energy density. Because $D_0(r)$ is brough forward the ELF as origin, what the ELF shows is an affiliate localization. The compounds of Si_5O_{10},

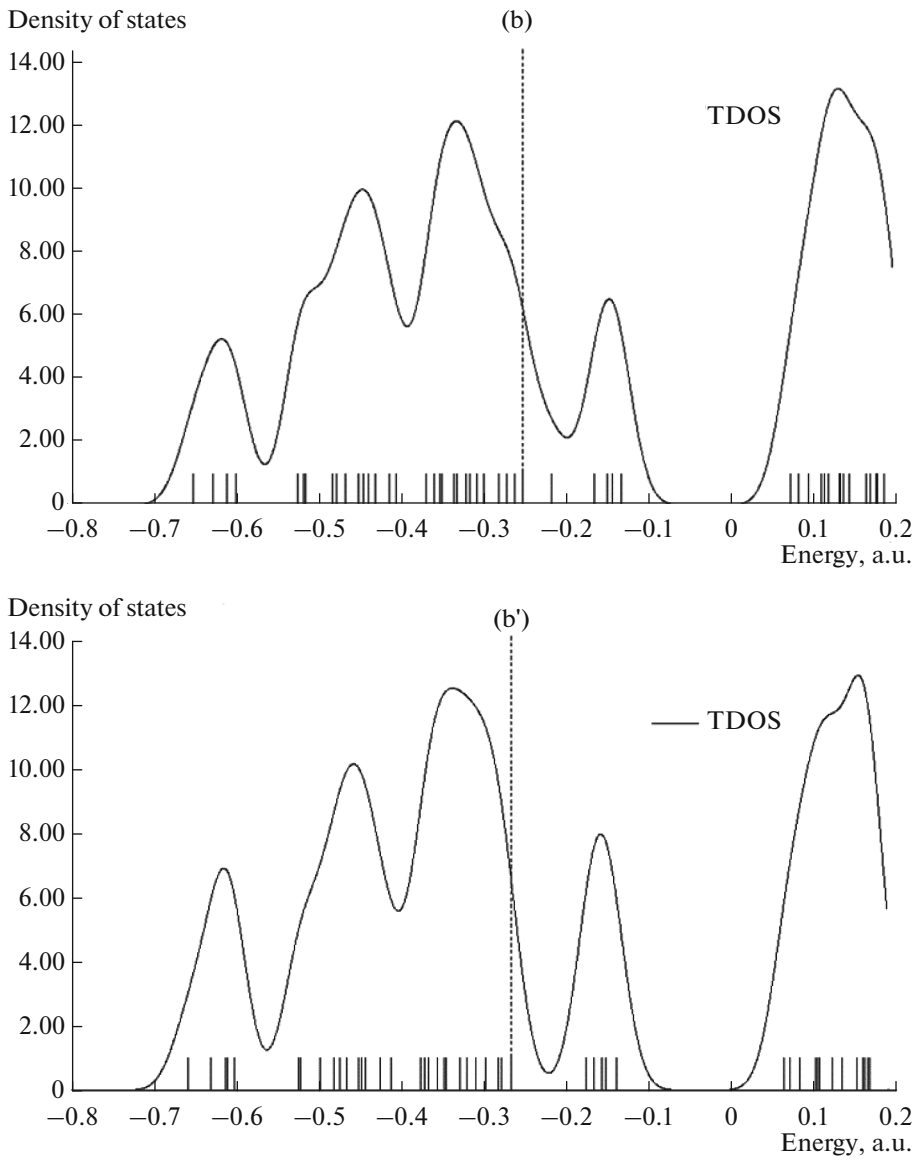

Fig. 3. (Contd.)

Ge_5O_{10}, and Si_5O_{10}–Ge_5O_{10} can be defined by ELF graphs owing to exploring their delocalization/localization characterizations of electrons and chemical bonds (Fig. 4).

A vaster jointed area engaged by an isosurface map for Si_5O_{10}–Ge_5O_{10} cluster (Fig.4c) means that electron delocalization in Si_5O_{10}–Ge_5O_{10} cluster toward H–Si_5O_{10}–Ge_5O_{10}–H (Fig. 4c') is easier than Si_5O_{10} with labeling atoms of O9, O10, Si13 (Fig. 4a) through hydrogen adsorption (Fig. 4a') with labeling atoms of O10, Si13, Si16 or Ge_5O_{10} (Fig. 4b) with labeling atoms of O9, O10, Ge13 during hydrogen adsorption (Fig. 4b') with labeling atoms of O10, Ge13, Ge16 and a narrower connected area occupied by an isosurface map means that electron delocalization is relatively difficult. In fact, the counter map of ELF can confirm that Si_5O_{10}–Ge_5O_{10} (Fig. 4c) cluster with labeling atoms of O10, Si13, Ge28 increases the efficiency during hydrogen adsorption towards formation of H–Si_5O_{10}–Ge_5O_{10}–H (Fig.4c') labeling atoms of Si13, Ge28, H31 or H32.

The changes of charge density analysis in the adsorption process have illustrated that Si_5O_{10} and Ge_5O_{10} have shown the Bader charge of −1.456 and −1.532 coulomb, respectively, before hydrogen adsorption and −1.471 and −1.565 coulomb, respectively, after hydrogen adsorption. Furthermore, Si_5O_{10}–Ge_5O_{10} has indicated the Bader charge of −1.578 coulomb before H adsorption and −2.276 coulomb after H adsorption. The differences of charge density for these structures are measured as: $\Delta Q_{Si_5O_{10}} = -0.015$,

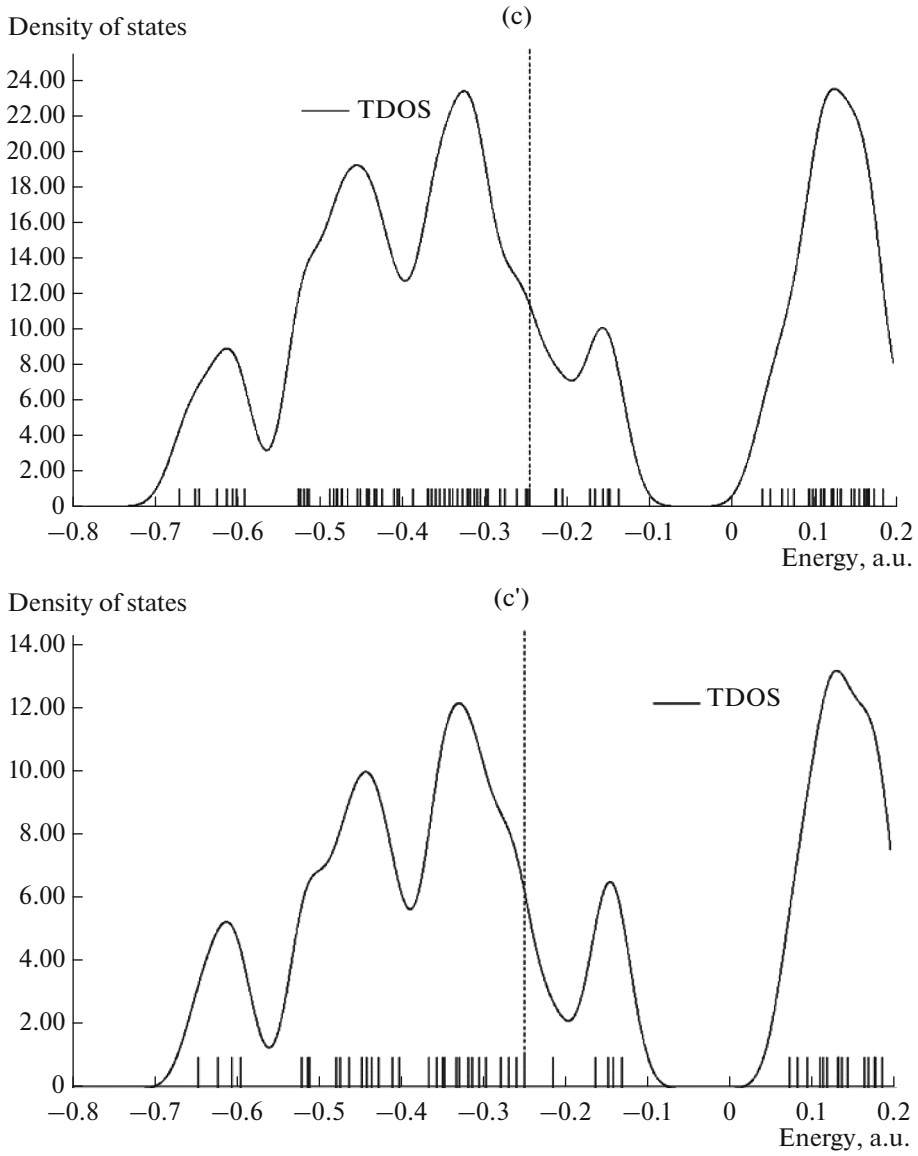

Fig. 3. (Contd.)

$\Delta Q_{Ge_5O_{10}} = -0.033$ and $\Delta Q_{Si_5O_{10}-Ge_5O_{10}} = -0.698$. Therefore, the results have shown that the cluster of Si_5O_{10}–Ge_5O_{10} has the most tensity and for electron accepting owing to hydrogen grabbing.

3.2. Theory of Nuclear Quadrupole Resonance

Hydrogen adsorption nanoclusters of Si_5O_{10} and Ge_5O_{10} under various electric potentials and were measured through NQR calculations. The NQR frequencies have been measured for Si_5O_{10}, H–Si_5O_{10}, Ge_5O_{10} and H–Ge_5O_{10} towards estimating the hydrated nanocluster of H–Si_5O_{10}–Ge_5O_{10}–H (Table 1). The NQR method is related to the multipole expansion in Cartesian coordinates as the equation [72–75]. In this research work, the electric potential as the quantity of work energy through carrying over the electric charge from one position to another position in the essence of electric field has been evaluated for Si_5O_{10}, H–Si_5O_{10}, Ge_5O_{10} and H–Ge_5O_{10} complexes (Table 1).

Si, Ge, O and hydrogen atoms absorbed on Si_5O_{10} and Ge_5O_{10} have been calculated through the Bader charge and electronic potential properties. The values detect that with augmenting the negative charge of various atoms, the electric potential extracted from NQR calculations grows. Besides, the elements of O2, O3, O7, O8, O9, O10, O11, O12, O14, O15 of Si_5O_{10} and Ge_5O_{10} have exhibited the most efficiency for admitting the electron from electron donor of H16 adsorbed on Si_5O_{10} and Ge_5O_{10} (Table 1). In Fig. 5, it

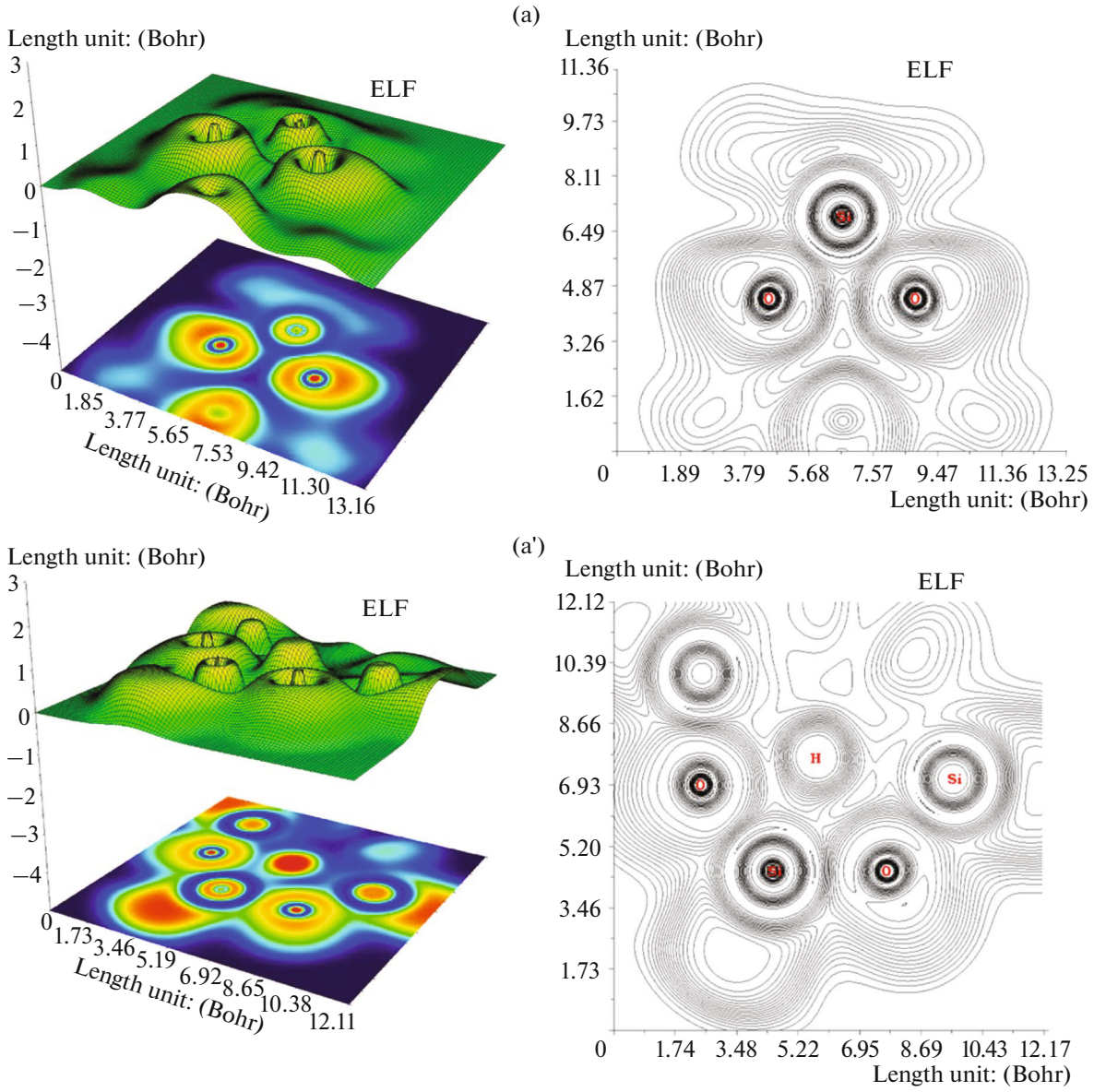

Fig. 4. The graphs of ELF for (a) Si_5O_{10}, (a') H–Si_5O_{10}, (b) Ge_5O_{10}, (b') H–Ge_5O_{10}, (c) Si_5O_{10}–Ge_5O_{10} and (c') H–Si_5O_{10}–Ge_5O_{10}–H. (Counter line map in the right and shaded surface map with projection in the left.)

has been sketched the electric potential of nuclear quadrupole resonance versus Bader charge for some atoms of Si, Ge, O and hydrogen atoms absorbed on Si_5O_{10} and Ge_5O_{10}. In Fig. 5a, it was observed the behavior of Si and O atoms in Si_5O_{10} with high sensitivity based on relation coefficient of $R^2 = 0.9999$; however, hydrogen adsorption on the Si_5O_{10} (H–Si_5O_{10}) has shown high sensitivity with relation coefficient of $R^2 = 0.9999$ (Fig. 5b). In Fig. 5c, it was observed the behavior of Ge and O atoms in Ge_5O_{10} and hydrogen adsorption on the Ge_5O_{10} (H–Ge_5O_{10}) (Fig. 5d) with high sensitivity of $R^2 = 1$. The fluctuated peaks for electric potential have been shown around hydrogen adsorption on the Si_5O_{10} and Ge_5O_{10} which demonstrates the electron accepting specifications of hydrogen versus the Si, Ge, O of Si_5O_{10} and Ge_5O_{10} (Figs. 5a, 5d). Besides, it can be considered that oxygen atoms in the functionalized Si_5O_{10} and Ge_5O_{10} might have more impressive sensitivity for accepting the electrons from H atoms in the process of adsorption mechanism. Based on the mentioned results, there can be renewed interest in combination of silicon and germanium as a nanocluster of Si_5O_{10}–Ge_5O_{10} for potential applications in next-generation electronics. Thus, it should be explored its unique properties, such as its ability to undergo a reversible phase transition, which could lead to advancements in electronic memory devices.

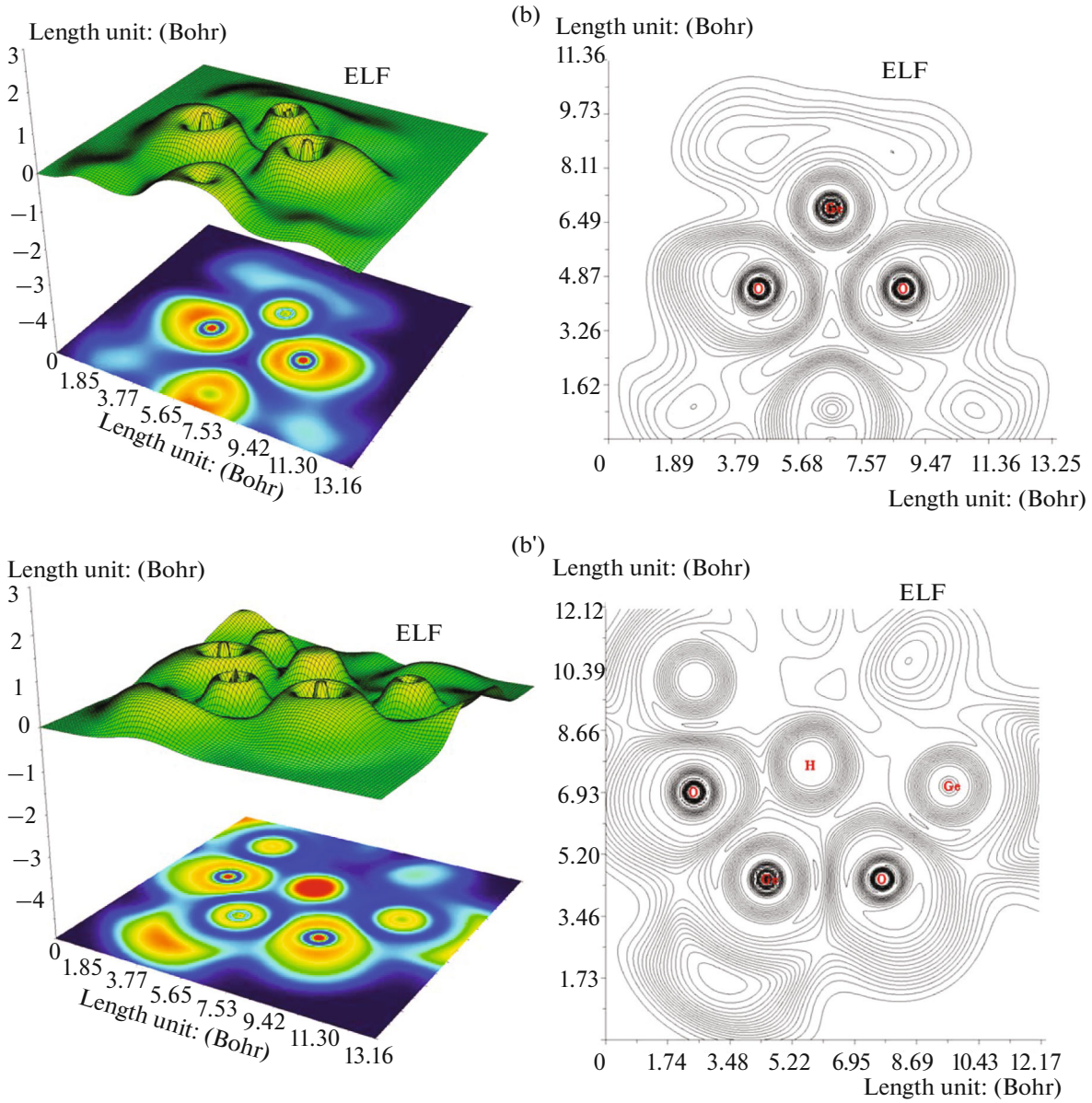

Fig. 4. (Contd.)

Previous literatures showed that the Pd–SiO_2 interfaces are responsible for hydrogen sensitivity of the Pd–SiO_2–Si structure [76], and Pd–SiO_2 interface supercells were utilized in order to evaluate the hydrogen-induced polarization at the Pd–SiO_2 interfaces [77]. Another study has indicated that the Ge(111)/a–GeO_2 and Ge(100)/a–GeO_2 interfaces have the lowest and highest interface energies, respectively. The stability of the Ge/a–GeO_2 interface is governed by the interfacial bond density and the minimization of the dangling bonds. We find that the interface region, composed of the Ge suboxides, dominates the electronic structures of the Ge/a–GeO_2. The Ge atoms with uncompensated dangling bonds result in various trap states within the band gap of Ge, which is related to the charge neutrality level of the Ge defect [78]. Our target in this sub-section has been studying the effect of electric potential results from NQR calculations for hydrogen adsorption on Si_5O_{10} and Ge_5O_{10} nanoclusters. Based on our results from Table 1 improved hydrogen storage can be obtained if hydrogen clusters are formed. Applied electric potential will introduce the charge to the nanoclusters of Si_5O_{10} and Ge_5O_{10} and hence can promote the opportunity for the formation of hydrogen clusters of H–Si_5O_{10} and H–$Ge_5O_{10,}$ respectively. The higher the applied electric potential is, the higher the hydrogen adsorption capacity (Figs. 5b, 5d).

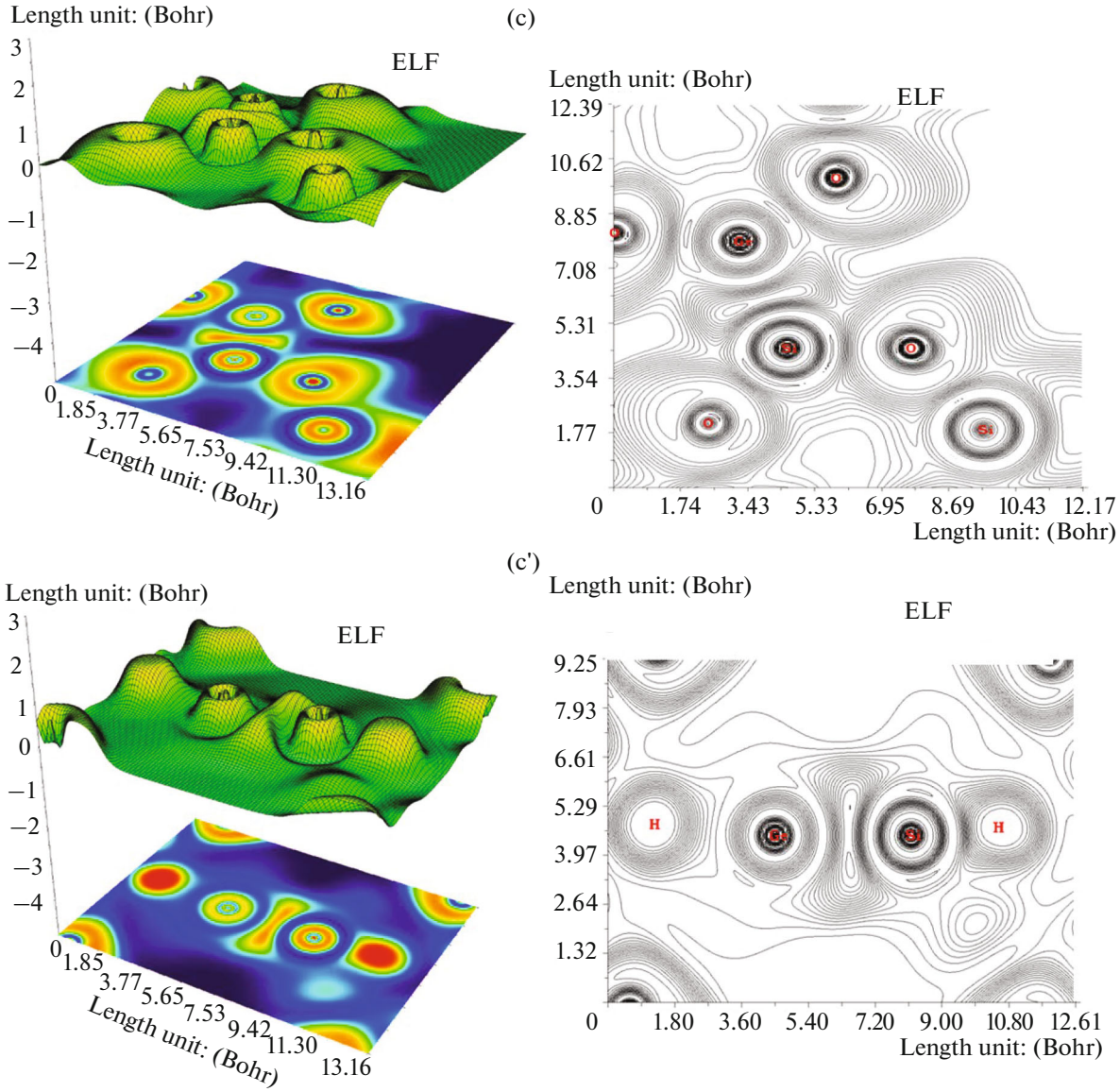

Fig. 4. (Contd.)

3.3. Analysis of Nuclear Magnetic Resonance Spectra

Based on the resulted amounts, nuclear magnetic resonance (NMR) spectra of Si_5O_{10} and Ge_5O_{10} complexes as the potential molecules for hydrogen storage can unravel the efficiency of these complexes for saving clean energy. From the DFT calculations, it has been attained the chemical shielding (CS) tensors in the principal axes system to estimate the isotropic chemical-shielding (CSI) and anisotropic chemical-shielding (CSA) [79]. The NMR data of isotropic (σ_{iso}) and anisotropic shielding tensors (σ_{aniso}) of hydrogen atoms adsorbed on Si_5O_{10} and Ge_5O_{10} complexes towards formation of H–Si_5O_{10} and H–Ge_5O_{10} complexes have been computed by Gaussian 16 revision C.01 program package [63] and been shown in Table 2.

In Table 2, NMR data has reported the notable amounts for hydrogen atoms which were adsorbed on Si_5O_{10} and Ge_5O_{10} complexes. The observed increase in the chemical shift anisotropy spans for H atoms adsorption on Si_5O_{10} and Ge_5O_{10} complexes are near O 2, O3, O7, O8, O12, O14 and O15. The notable fragile signal intensity close to the parallel edge of the nanocluster sample might be owing to silicon or germanium binding induced non-spherical distribution of these clusters. Figure 6 exhibited the same tendency of shielding for silicon or germanium; however, a considerable deviation exists from doping atoms of O2, O3, O7, O8, O12, O14 and O15 through interaction

Table 1. The electric potential (E_p/a.u.) and Bader charge (Q/coulomb) through NQR calculation for Si_5O_{10}, $H{-}Si_5O_{10}$, Ge_5O_{10} and $H{-}Ge_5O_{10}$ complexes

Si_5O_{10}			$H{-}Si_5O_{10}$			Ge_5O_{10}			$H{-}Ge_5O_{10}$		
atom	Q	E_p	atom	Q	E_p	atom	Q	E_p	atom	Q	E_p
Si1	1.42	−49.09	Si1	1.44	−49.08	Ge1	1.49	−155.04	Ge1	1.52	−155.04
O2	−0.62	−22.29	O2	−0.62	−22.29	O2	−0.66	−22.31	O2	−0.65	−22.32
O3	−0.79	−22.33	O3	−0.75	−22.31	O3	−0.83	−22.35	O3	−0.78	−22.33
Si4	1.42	−49.09	Si4	1.43	−49.09	Ge4	1.50	−155.05	Ge4	1.51	−155.04
Si5	1.42	−49.09	Si5	1.44	−49.09	Ge5	1.49	−155.05	Ge5	1.52	−155.04
Si6	1.42	−49.09	Si6	1.43	−49.08	Ge6	1.49	−155.05	Ge6	1.51	−155.04
O7	−0.65	−22.30	O7	−0.68	−22.33	O7	−0.68	−22.32	O7	−0.72	−22.34
O8	−0.79	−22.33	O8	−0.74	−22.30	O8	−0.83	−22.35	O8	−0.77	−22.32
O9	−0.73	−22.31	O9	−0.74	−22.32	O9	−0.77	−22.33	O9	−0.78	−22.34
O10	−0.76	−22.34	O10	−0.74	−22.32	O10	−0.80	−22.36	O10	−0.78	−22.35
O11	−0.76	−22.34	O11	−0.73	−22.34	O11	−0.80	−22.36	O11	−0.78	−22.36
O12	−0.74	−22.31	O12	−0.73	−22.32	O12	−0.78	−22.33	O12	−0.76	−22.34
Si13	1.45	−49.09	Si13	1.47	−49.08	Ge13	1.53	−155.05	Ge13	1.56	−155.04
O14	−0.64	−22.30	O14	−0.64	−22.30	O14	−0.67	−22.31	O14	−0.70	−22.33
O15	−0.63	−22.29	O15	−0.68	−22.34	O15	−0.66	−22.31	O15	−0.69	−22.35
			H16	−0.15	−0.77				H6	−0.20	−0.784

Table 2. Data of NMR shielding tensors (ppm) for selected atoms of Si_5O_{10}, $H{-}Si_5O_{10}$, Ge_5O_{10} and $H{-}Ge_5O_{10}$ complexes

Si_5O_{10}			$H{-}Si_5O_{10}$			Ge_5O_{10}			$H{-}Ge_5O_{10}$		
atom	σ_{iso}	σ_{aniso}	atom	σ_{iso}	σ_{aniso}	atom	σ_{iso}	σ_{aniso}	atom	σ_{iso}	σ_{aniso}
Si1	554.06	419.08	Si1	636.08	83.31	Ge1	11774.57	78310.40	Ge1	2269.96	265.46
O2	48.40	1103.17	O2	197.71	180.52	O2	7981.03	45129.91	O2	185.77	323.78
O3	719.20	1393.84	O3	213.90	571.64	O3	26849.60	102235.88	O3	235.00	690.97
Si4	606.85	283.53	Si4	612.49	136.09	Ge4	2860.04	56431.23	Ge4	2254.92	354.40
Si5	515.08	300.30	Si5	590.56	112.09	Ge5	22560.33	50034.95	Ge5	2196.23	239.01
Si6	499.44	298.51	Si6	640.61	109.00	Ge6	25249.19	67283.27	Ge6	2283.05	294.68
O7	165.28	1989.85	O7	257.47	540.46	O7	28391.88	116633.36	O7	192.29	265.99
O8	446.38	1626.01	O8	345.30	760.80	O8	19250.32	151688.34	O8	400.69	945.35
O9	644.00	1145.01	O9	396.42	516.76	O9	8016.65	16619.93	O9	429.44	692.57
O10	258.21	801.06	O10	291.98	500.11	O10	12714.21	20281.55	O10	322.28	641.07
O11	59.31	646.45	O11	381.78	579.44	O11	9151.57	14760.91	O11	363.38	661.78
O12	777.76	1673.73	O12	592.88	761.13	O12	45077.01	82973.35	O12	644.30	1039.24
Si13	676.74	69.96	Si13	700.35	80.46	Ge13	1836.03	6719.10	Ge13	2377.42	144.00
O14	644.64	1598.29	O14	192.65	365.70	O14	21908.37	61863.15	O14	93.65	302.72
O15	640.66	1233.63	O15	575.73	737.13	O15	6288.94	33932.60	O15	458.00	712.97
			H16	33.88	5.14				H16	38.01	2.78

with hydrogen atoms during adsorbing on Si_5O_{10} and Ge_5O_{10} complexes.

NMR spectroscopy has shown the gap chemical shielding between silicon and oxygen in Si_5O_{10} (Fig. 6a), hydrogen, silicon and oxygen in $H{-}Si_5O_{10}$ (Fig. 6b), germanium and oxygen in Ge_5O_{10} (Fig.6c), hydrogen, germanium and oxygen in $H{-}Ge_5O_{10}$ (Fig. 6d). The yield of electromagnetic shifting can be

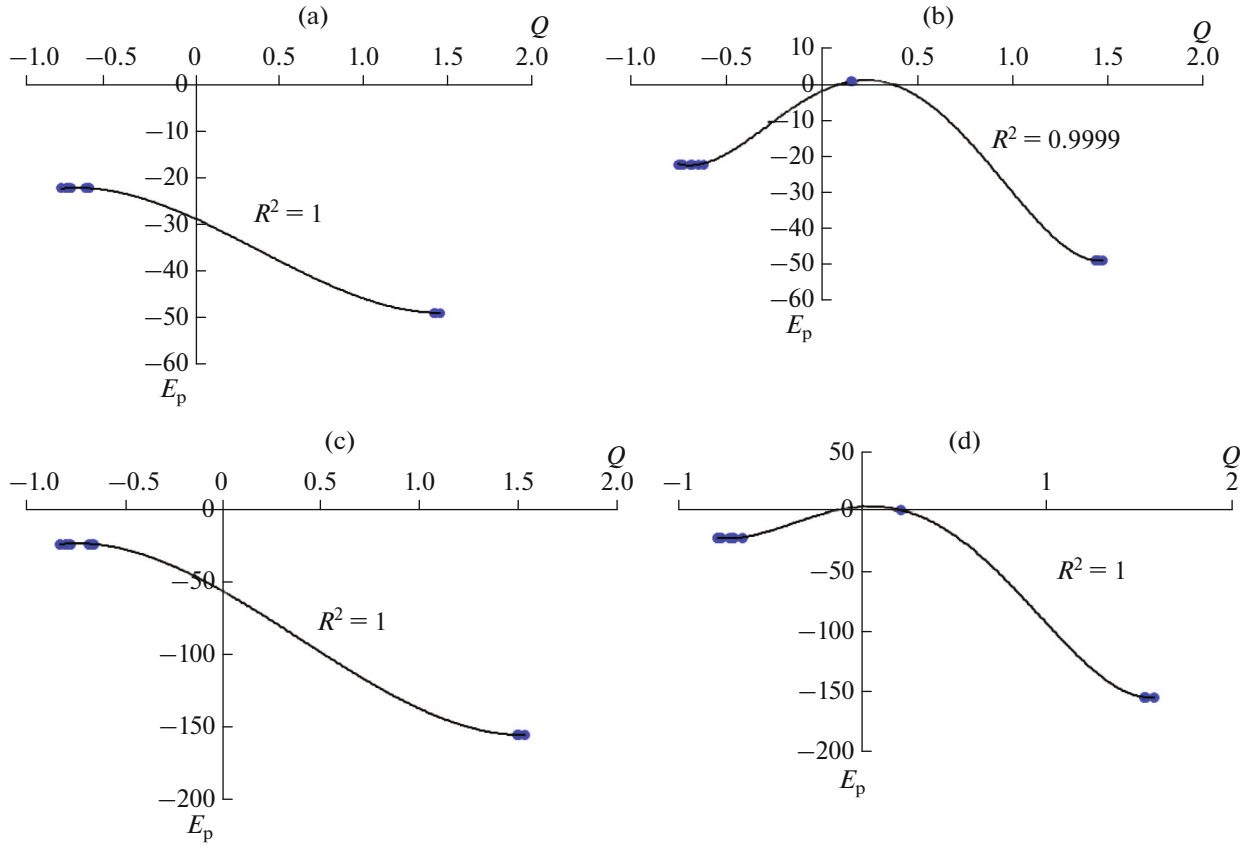

Fig. 5. Electric potential (a.u.) versus Bader charge (coulomb) through NQR calculation for (a) Si_5O_{10}, (b) $H–Si_5O_{10}$, (c) Ge_5O_{10} and (d) $H–Ge_5O_{10}$.

directed by oxygen atoms of O3, O7, O12, O14 in Si_5O_{10} (Fig. 6a), O3, O8, O12, O15 in $H–Si_5O_{10}$ (Fig. 6b), O3, O8, O12, O14 in Ge_5O_{10} (Fig. 6c), and Ge1, Ge4, Ge5, Ge6, Ge13 in $H–Ge_5O_{10}$ (Fig. 6d). The results have shown that the intensity for hydrogen adsorption can be developed in Ge_5O_{10} through germanium atoms compared to silicon atoms in Si_5O_{10}. Although both silicon and germanium are semiconductor elements, germanium can be more conductive than silicon in cell batteries due to high semiconducting properties. Therefore, it can be promised that the adapted outcomes would be advantageous in modelling a novel $Si_5O_{10}–Ge_5O_{10}$ complex for increasing the adsorption of hydrogen atoms in cell batteries based on their structural studies.

An NMR investigation aiming at clarifying the internal arrangement and diffusion properties of hydrogen molecules inside functionalized porous silica materials was achieved by a research article. Indeed, by properly tuning surface interactions and the textural characteristics, the overall efficiency of H_2 capture processes could be improved. The NMR spectral analysis and the T1 relaxation times indicated two different populations for H_2 sorbate due to the molecules adsorbed in mesopores and in micropores. The spin-echo decay revealed two different diffusion mechanisms coexist in the functionalized mesoporous silica, except for the material functionalized groups, which shows a single diffusion coefficient [80]. Figures 6a and 6c clarifies that significative NMR peaks for heteroclusters of Si_5O_{10} and Ge_5O_{10} before H_2 adsorption, respectively. However, after hydrogen adsorption each peak only originates from H_2 filling the material pores Figs. 6b and 6d. All the proton signals are very broad and asymmetric. The latter feature, which is commonly observed in the case of multicomponent configurations indicates that different H_2 populations coexist in a rapid exchange on the NMR timescale.

3.4. Insight of Infrared Spectroscopy and Thermochemistry

The infrared spectroscopy (IR) has been performed for hydrogen grabbing by Si_5O_{10} and Ge_5O_{10} nanoclusters. Therefore, it has been simulated the several clusters containing Si_5O_{10} (Fig. 7a), $H–Si_5O_{10}$ (Fig. 7b), Ge_5O_{10} (Fig. 7c), and $H–Ge_5O_{10}$ (Fig. 7d). The frequency values through the IR curves between 200–1100 cm^{-1} have been achieved for Si_5O_{10} with

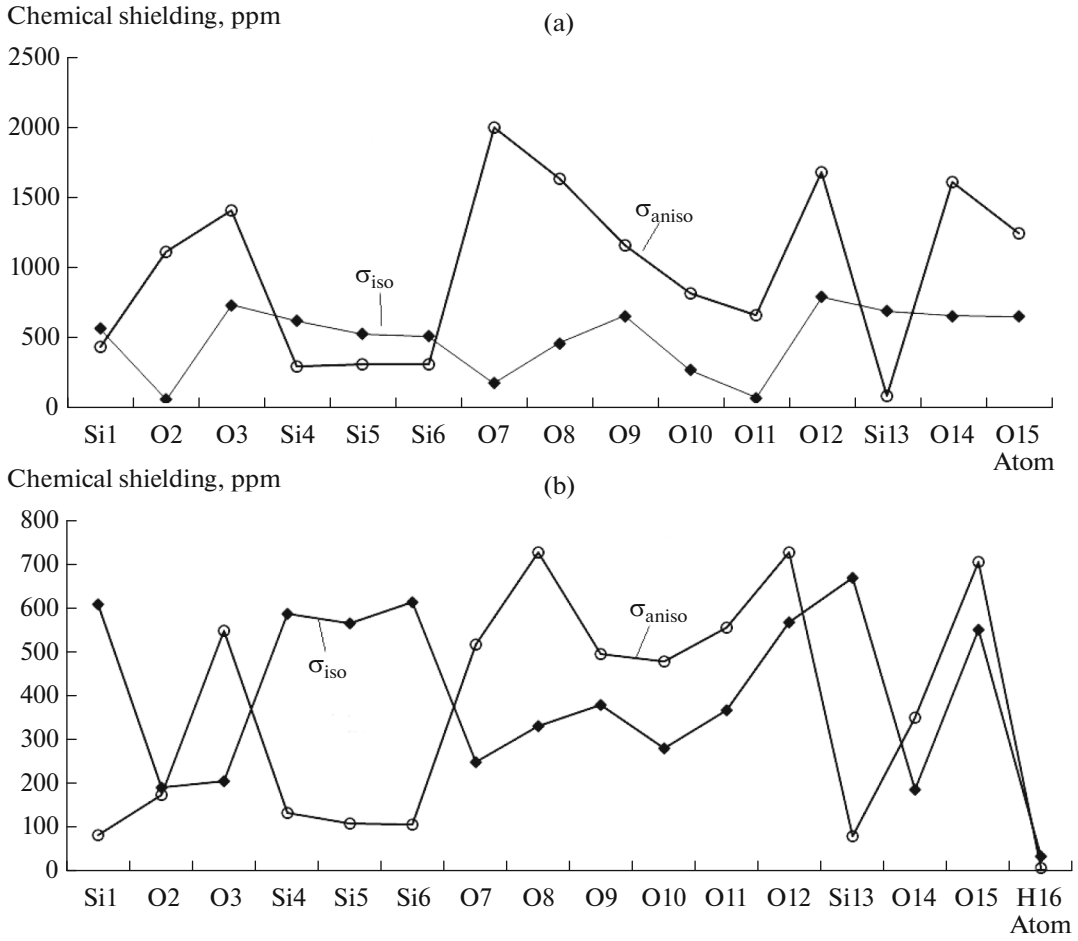

Fig. 6. The NMR spectra for (a) Si_5O_{10}, (b) H–Si_5O_{10}, (c) Ge_5O_{10}, and (d) H–Ge_5O_{10} complexes.

several sharp peaks around 371.52, 400.69, 616.11, 736.73, 746.09, 784.99 and 84.75 cm^{-1} (Fig. 7a). Moreover, Fig. 7a has shown the frequency range between 300–1200 cm^{-1} for H–Si_5O_{10} with sharp peaks around 464.86, 663.71, 702.49, 832.17, 841.00 and 1126.17 cm^{-1}. Figure 7b has indicated the fluctuation of frequency between 200–1200 cm^{-1} for Ge_5O_{10} with sharp peaks around 364.39, 610.61, 780.37 and 1022.67 cm^{-1}. Furthermore, the graph of Fig. 7b has been observed in the frequency range between 200–1200 cm^{-1} for H–Ge_5O_{10} with several sharp peaks around 793.72, 814.41, 1003.50 and 1021.96 cm^{-1}. Hydrogen capture with Si_5O_{10} and Ge_5O_{10} nanoclusters has described that the frame of the overcoming cluster is related to Ge_5O_{10} in the high amounts of frequency. This property makes germanium potentially advantageous for certain high-frequency applications requiring faster cell battery switching speeds. The advantages of germanium over silicon include its higher electron and hole mobility, allowing germanium devices to operate at higher frequencies than silicon devices.

Figures 7a, 7b summarized the results obtained from Gaussian 16 revision C.01 program package [63] by IR-spectroscopy extracted from GaussView 6.1 [64] applied in a reflection-geometry to metalloid oxides of Si_5O_{10}, Ge_5O_{10} and Si_5O_{10}–Ge_5O_{10}. H-binding interactions with Si_5O_{10}, Ge_5O_{10} and Si_5O_{10}–Ge_5O_{10} nanoclusters lead to significant changes in the IR spectrum, like frequency shifts of the order of magnitude of cm^{-1} and increases of IR intensity for bands related to vibrational modes of functional groups. In addition, for metalloid oxides of Si_5O_{10}, Ge_5O_{10} and Si_5O_{10}–Ge_5O_{10}, absorbance bands caused by excitation of adsorbate vibrations are always positive and excitation of the vibration leads to a decrease in reflected intensity. This can be understood by considering that, the supporting Si_5O_{10}–Ge_5O_{10} acts as a mirror and increases the total intensity of the reflected IR frequency to a value which is comparable to that for Si_5O_{10} and Ge_5O_{10}. Furthermore, the Si5O10 nanocluster has shown two sharp peaks after hydrogen adsorption and formation of hydrated nanocluster of H–Si_5O_{10} (Fig. 7a). These frequencies belong to the high intensity of vibrational modes 129, 161, 177.

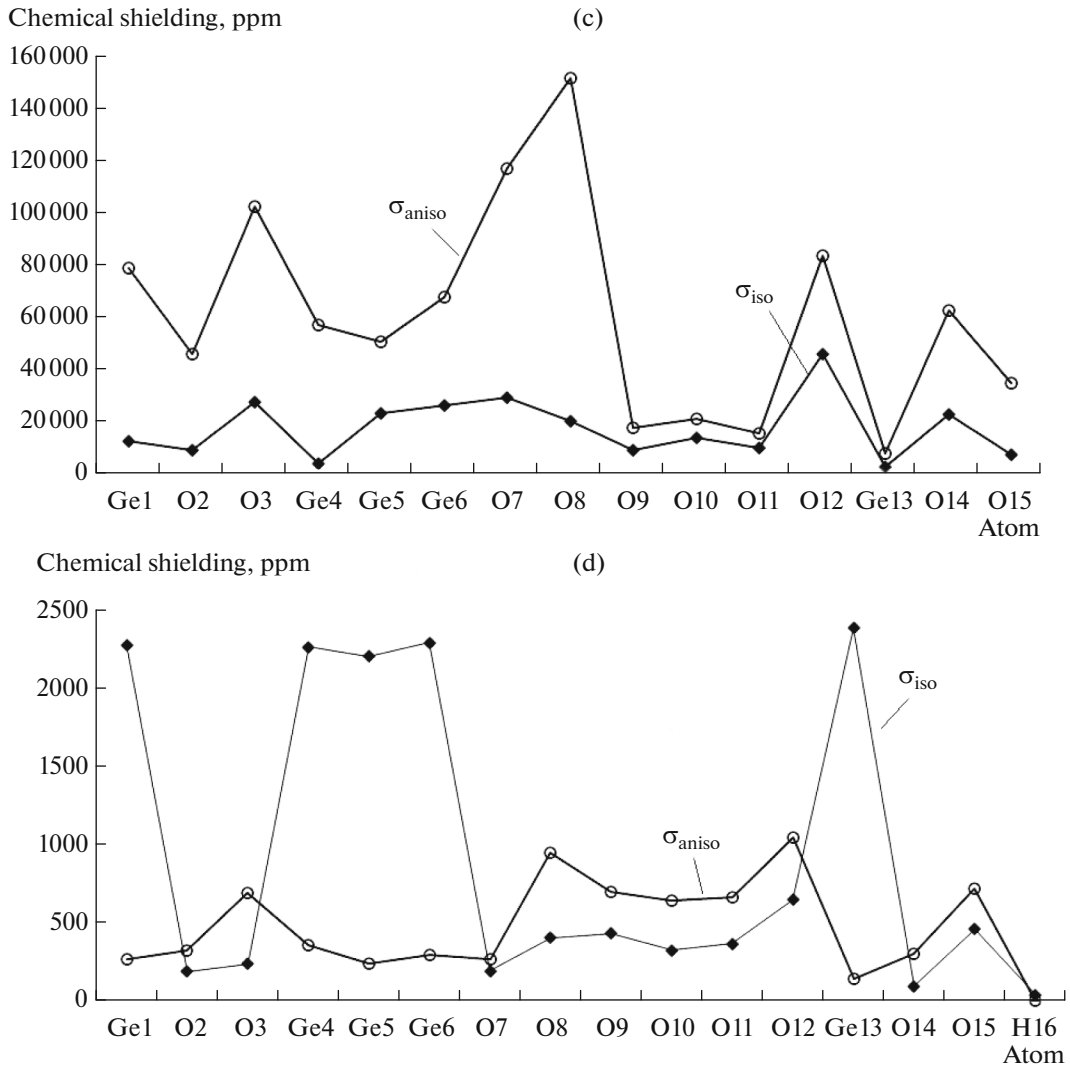

Fig. 6. (Contd.)

Besides, the Ge_5O_{10} nanocluster has exhibited four remarkable peaks around vibrational intensity modes of 111, 114, 146, 294 after hydrogen adsorption which forms the hydrated nanocluster of $H–Ge_5O_{10}$ (Fig. 7b).

Table 3 through the thermodynamic specifications concluded that $Si_5O_{10}–Ge_5O_{10}$ nanocluster might be a more efficient structure for hydrogen trapping. Thermodynamic parameters of hydrogen adsorption on Si_5O_{10}, Ge_5O_{10}, and $Si_5O_{10}–Ge_5O_{10}$ nanoclusters have been assigned through a given number of hydrogen donor sites, the stabilities of linkage of two complexes of Si_5O_{10}, Ge_5O_{10} and formation of $Si_5O_{10}–Ge_5O_{10}$ nanocluster can be considered as: $H–Si_5O_{10}–Ge_5O_{10}–H > Si_5O_{10}–Ge_5O_{10} > H–Ge_5O_{10} > Ge_5O_{10} > H–Si_5O_{10} > Si_5O_{10}$ complexes (Table 3). The changes of Gibbs free energy versus dipole moment could detect the maximum efficiency of $Si_5O_{10}–Ge_5O_{10}$ for hydrogen adsorption through ΔG^{o}_{ads} which is related to linkage between hydrogen atoms with silicon and germanium in $Si_5O_{10}–Ge_5O_{10}$ and formation of hydrated nanocluster of $H–Si_5O_{10}–Ge_5O_{10}–H$ (Fig. 8).

There is a wide range of energies contributing to the free energy of adsorption, which can be grouped into non-electrostatic and electrostatic:

$$\Delta G^{o}_{ads} = \Delta G^{o}_{non-elect} + \Delta G^{o}_{elect}, \text{ see Eq.} \quad (6)$$

Although at atomic levels, all ionic and molecular interactions can be interpreted as electric, this term is restricted to coulombic interactions and all other interactions are termed non-electrostatic, whatever their origin. These interactions, either attractive or repulsive, are strongly dependent on the charge densities for both the $Si_5O_{10}–Ge_5O_{10}$ surface and the adsorptive molecule of hydrogen. The non-electrostatic interactions are always attractive, and include van der Waals forces, hydrophobic interactions and

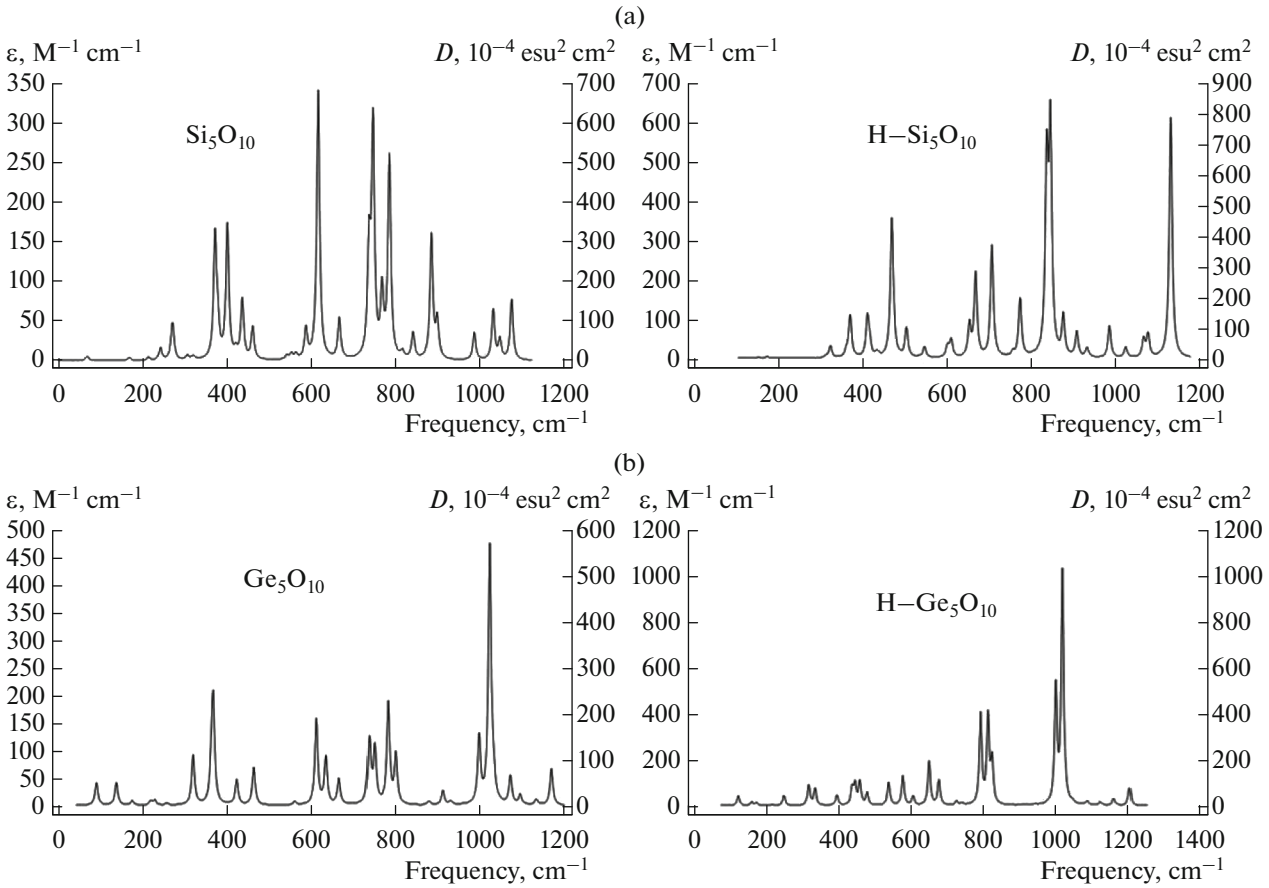

Fig. 7. The Frequency (cm^{-1}) changes through the IR spectra for (a) Si_5O_{10}, and H–Si_5O_{10} and (b) Ge_5O_{10} & H–Ge_5O_{10} nanoclusters. [Note: ε (M^{-1} cm^{-1}) is the absorbance unit and D (10^{-4} esu^2 cm^2) is the dipole strength via the esu or electrostatic unit, which is a unit of charge in the cgs (centimeter-gram-second system)].

hydrogen bonding. So, the adsorption process of hydrogen atoms on Si_5O_{10}, Ge_5O_{10}, and Si_5O_{10}–Ge_5O_{10} nanoclusters is affirmed by the ΔG^{o}_{ads} quantity:

$$\Delta G^{o}_{ads/Si_5O_{10}} = \Delta G^{o}_{H-Si_5O_{10}} - \left(\Delta G^{o}_{Si_5O_{10}} + \Delta G^{o}_{H}\right), \quad (7)$$

$$\Delta G^{o}_{ads/Ge_5O_{10}} = \Delta G^{o}_{H-Ge_5O_{10}} - \left(\Delta G^{o}_{Ge_5O_{10}} + \Delta G^{o}_{H}\right), \quad (8)$$

$$\Delta G^{o}_{ads/Si_5O_{10}-Ge_5O_{10}} = \Delta G^{o}_{H-Si_5O_{10}-Ge_5O_{10}-H} - \left(\Delta G^{o}_{Si_5O_{10}} + \Delta G^{o}_{H-Si_5O_{10}} + \Delta G^{o}_{Ge_5O_{10}} + \Delta G^{o}_{H-Ge_5O_{10}}\right). \quad (9)$$

Table 3. The thermodynamic characters of Si_5O_{10}, H–Si_5O_{10}, Ge_5O_{10}, H–Ge_5O_{10}, Si_5O_{10}–Ge_5O_{10} and H–Si_5O_{10}–Ge_5O_{10}–H nanoclusters using CAM–B3LYP–D3/6-311+G(d, p) calculation

Compound	Dipole moment, Debye	$\Delta E^{o}_{ads} \times 10^{-3}$, kcal/mol	$\Delta H^{o}_{ads} \times 10^{-3}$, kcal/mol	$\Delta G^{o}_{ads} \times 10^{-3}$, kcal/mol	$E^{o}_{H\text{-binding}}$, kcal/mol
Si_5O_{10}	0.4437	−1379.64	−1379.64	−1379.64	$-0.29 \times 10^{+3}$
H–Si_5O_{10}	0.7333	−1379.93	−1379.93	−1379.96	
Ge_5O_{10}	0.8029	−6981.16	−6981.16	−6981.20	$-0.27 \times 10^{+3}$
H–Ge_5O_{10}	0.5883	−6981.44	−6981.44	−6981.47	
Si_5O_{10}–Ge_5O_{10}	1.2754	−8360.86	−8360.86	−8360.89	$-0.50 \times 10^{+3}$
H–Si_5O_{10}–Ge_5O_{10}–H	1.5386	−8361.37	−8361.37	−8361.39	

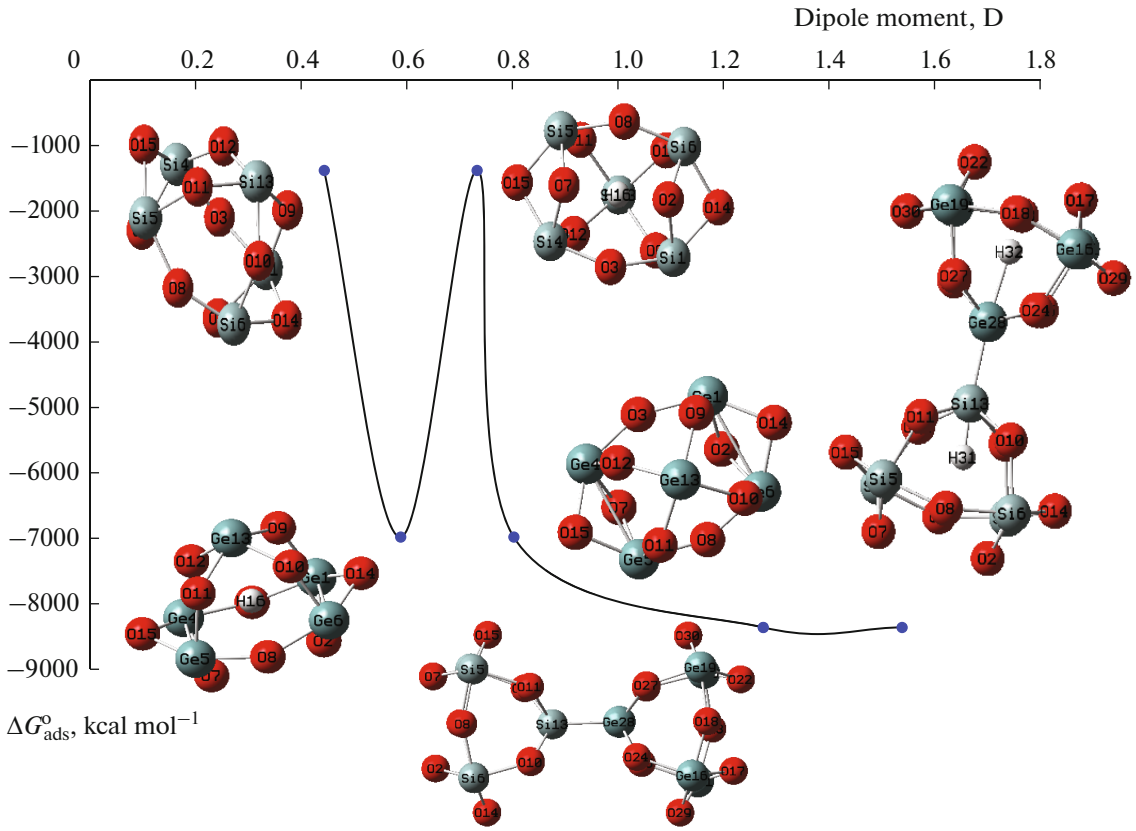

Fig. 8. Gibbs free energy (ΔG^{o}_{ads}) for Si_5O_{10}, H–Si_5O_{10}, Ge_5O_{10}, H–Ge_5O_{10}, Si_5O_{10}–Ge_5O_{10} and H–Si_5O_{10}–Ge_5O_{10}–H nanoclusters.

Based on the Eqs. (13)–(15), the values of hydrogen binding ($E^{o}_{H\text{-binding}}$) by adsorbents of Si_5O_{10}, Ge_5O_{10} and Si_5O_{10}–Ge_5O_{10} nanoclusters have been reported in Table 3 as $-0.29 \times 10^{+3}$, $-0.27 \times 10^{+3}$ and $-0.5 \times 10^{+3}$ kcal/mol, respectively. Figure 8 has shown the key role of interaction between the adsorbate of hydrogen atoms as the electron donors and the adsorbent of Si_5O_{10}, Ge_5O_{10} and Si_5O_{10}–Ge_5O_{10} nanoclusters as the electron acceptors. Moreover, germanium also has interesting optical properties, including transparency to infrared radiation. This characteristic makes it valuable in the production of lenses for thermal imaging systems and night vision devices. Its use extends to fiber optics, where it serves as a dopant to enhance the refractive index of optical fibers, improving signal transmission. Metal oxides have shown great potential as coating candidates due to their high electric conductivity, ability to enhance structural stability and good electrochemical performance when compared to the majority of other surface modifications. So, various aspects in relation to performance enhancement effects of different metal oxides that are used as coatings on materials for hydrogen adsorption properties are essential. Hence, formation of composites by combining two or more compatible materials in the hopes of enhancing thermodynamic properties of functional materials for energy storage and superior performance is remarkable. Finally, combination of Si_5O_{10} and Ge_5O_{10} and producing Si_5O_{10}–Ge_5O_{10} nanocluster can promise enhancing hydrogen storage in the cell batteries through formation of the hydrated cluster of H–Si_5O_{10}–Ge_5O_{10}–H. The heteroclusters of Si_5O_{10}, Ge_5O_{10}, and Si_5O_{10}–Ge_5O_{10} have the lowest and highest interface energies, respectively. The stability of Si_5O_{10}, Ge_5O_{10}, and Si_5O_{10}–Ge_5O_{10} interfaces is governed by the interfacial bond density and the minimization of the dangling bonds.

CONCLUSIONS

In summary, H-grabbing on the nanoclusters of Si_5O_{10}, Ge_5O_{10} and Si_5O_{10}–Ge_5O_{10} was investigated by first-principle calculations. The alterations of charge density illustrated a remarkable charge transfer towards Si_5O_{10}, Ge_5O_{10} and Si_5O_{10}–Ge_5O_{10} which might play the electron acceptor roles while H-atoms act as the stronger electron donner through adsorption on the Si_5O_{10}, Ge_5O_{10} and Si_5O_{10}–Ge_5O_{10}. As a matter of fact, Si_5O_{10}, Ge_5O_{10} and Si_5O_{10}–Ge_5O_{10} have greater interaction energy from Van der Waals' forces

with H-atoms that can cause them to be much more resistant. Besides, thermodynamic parameters describing H-grabbing on the nano-carbides of Si_5O_{10}, Ge_5O_{10} and Si_5O_{10}–Ge_5O_{10} have been investigated including internal process of the adsorbent–adsorbate system. As germanium has shown interesting optical properties, including transparency to infrared radiation, combination of Si_5O_{10} and Ge_5O_{10} and producing Si_5O_{10}–Ge_5O_{10} nanocluster can promise enhancing hydrogen storage in the cell batteries through formation of the hydrated cluster of H–Si_5O_{10}–Ge_5O_{10}–H. The amounts of hydrogen adsorption Si_5O_{10}, Ge_5O_{10} and Si_5O_{10}–Ge_5O_{10} nanoclusters have been estimated as -0.29×10^{-3}, -0.27×10^{-3} and -0.5×10^{-3} kcal/mol, respectively. Stability energy of hydrogen adsorption has indicated a detailed molecular model for atom–atom interactions and a distribution of point charges which can be utilized to reproduce the polarity of the solid material and the adsorbing molecules. Today, it is crucial to distinguish the potential of hydrogen technologies and bring up all perspectives of their performance, from technological progresses to economic and social effects. The authors intend to pursue research on sustainability and clean energy subjects towards finding new solutions for reducing the global dependency on fossil fuels.

ACKNOWLEDGMENTS

In successfully completing this paper and its research, the authors are grateful to Kastamonu University.

FUNDING

This work was supported by ongoing institutional funding. No additional grants to carry out or direct this particular research were obtained.

CONFLICT OF INTEREST

The authors of this work declare that they have no conflicts of interest.

REFERENCES

1. E. N. Antonov, A. G. Ivanova, L. I. Krotova, et al., Russ. J. Phys. Chem. B **17**, 1555–1560 (2023). https://doi.org/10.1134/S199079312308002X
2. F. Mollaamin, Russ. J. Phys. Chem. B **18**, 805–820 (2024). https://doi.org/10.1134/S1990793124700131
3. M. Monajjemi, M. T. Baie, and F. Mollaamin, Russ. Chem. Bull. **59**, 886–889 (2010). https://doi.org/10.1007/s11172-010-0181-5
4. F. Mollaamin, S. Mohammadi, Z. Khalaj, et al., Russ. J. Phys. Chem. B **18**, 67–82 (2024). https://doi.org/10.1134/S1990793124010330
5. V. Y. Agroskin, B. G. Bravy, G. K. Vasiliev, et al., Russ. J. Phys. Chem. B **17**, 1265–1269 (2023). https://doi.org/10.1134/S1990793123060131
6. A. Tahan, F. Mollaamin, and M. Monajjemi, Russ. J. Phys. Chem. A **83**, 587–597 (2009). https://doi.org/10.1134/S003602440904013X
7. S. Shahriari, M. Monajjemi, F. Mollaamin, J. Chil. Chem. Soc. **67**, 5468–5476 (2022). https://doi.org/10.4067/S0717-97072022000205468
8. A. M. Tereza, G. L. Agafonov, E. K. Anderzhanov, et al., Russ. J. Phys. Chem. B **17**, 1294–1299 (2023). https://doi.org/10.1134/S1990793123060246
9. V. I. Petinov, V. M. Timin, K. V. Bozhenko, et al., Russ. J. Phys. Chem. B **18**, 365–368 (2024). https://doi.org/10.1134/S1990793124020301
10. A. M. Tereza, G. L. Agafonov, E. K. Anderzhanov et al., Russ. J. Phys. Chem. B **17**, 974–978 (2023). https://doi.org/10.1134/S1990793123040309
11. M. A. A. Zadeh, H. Lari, L. Kharghanian, et al., J. Comput. Theor. Nanosci. **12**, 4358 (2015). doi org/ https://doi.org/10.1166/jctn.2015.4366
12. E. I. Rudenko, N. V. Dohlikova, A. K. Gatin, et al., Russ. J. Phys. Chem. B **17**, 845–852 (2023). https://doi.org/10.1134/S1990793123040164
13. E. M. Sarasia, S. Afsharnezhad, B. Honarparvar, et al., Phys. Chem. Liq. **49**, 561–571 (2011). https://doi.org/10.1080/00319101003698992
14. M. Monajjemi, H. Yamola, and F. Mollaamin, Fullerenes Nanotubes Carbon Nanostruct. **22**, 595–603 (2014). https://doi.org/10.1080/1536383X.2012.702163
15. F. Mollaamin, F. Najafi, M. Khaleghian, B. Khalili Hadad, and M. Monajjemi, Fullerenes Nanotubes Carbon Nanostruct. **19**, 653–667 (2011). https://doi.org/10.1080/1536383X.2010.504956
16. S. Shahriari, M. Monajjemi and K. Zare, Biointerface Res. Appl. Chem. **8**, 3219–3223 (2018).
17. R. R. Kayumov, A. P. Radaeva, A. A. Krupina, et al., Russ. J. Phys. Chem. B **17**, 801–809 (2023). https://doi.org/10.1134/S1990793123040097
18. M. Khaleghian, M. Zahmatkesh, F. Mollaamin, et al., Fullerenes Nanotubes Carbon Nanostruct. **19**, 251–261 (2011). https://doi.org/10.1080/15363831003721757
19. K. Y. Troshin, N. M. Rubtsov, G. I. Tsvetkov, et al., Russ. J. Phys. Chem. B **17**, 979–985 (2023). https://doi.org/10.1134/S1990793123040310
20. K. Y. Troshin, N. M. Rubtsov, G. I. Tsvetkov, et al., Russ. J. Phys. Chem. B **17**, 433–438 (2023). https://doi.org/10.1134/S1990793123020185
21. Q. Q. Xiong, Russ. J. Phys. Chem. B **18**, 638–644 (2024). https://doi.org/10.1134/S1990793124700155
22. F Mollaamin and M. Monajjemi, J. Comput. Theor. Nanosci. **12**, 1030–1039 (2015). https://doi.org/10.1166/jctn.2015.3846
23. X. Yuan, X.Tan, and B. Liu, Russ. J. Phys. Chem. B **17**, 886–895 (2023). https://doi.org/10.1134/S1990793123040322

24. L. I. Trakhtenberg, Russ. J. Phys. Chem. B **17**, 600–607 (2023). https://doi.org/10.1134/S1990793123030144
25. K. Bakhshi, F. Mollaamin, and M. Monajjemi, J. Comput. Theor. Nanosci. **8**, 763–768 (2011). https://doi.org/10.1166/jctn.2011.1750
26. F. Mollaamin, M. Monajjemi, S. Salemi, et al., Fullerenes Nanotubes Carbon Nanostruct. **19**, 182 (2011). https://doi.org/10.1080/15363831003782932
27. M. Monajjemi, M. Khaleghian, N. Tadayonpour, et al., Int. J. Nanosci. **09**, 517–529 (2010). https://doi.org/10.1142/S0219581X10007071
28. F. Mollaamin and M. Monajjemi, J. Cluster Sci. **34**, 2901–2918 (2023). https://doi.org/10.1007/s10876-023-02436-5
29. N. Yodsin, H. Sakagami, T. Udagawa, et al., Mol. Catal. **504**, 111486 (2021). https://doi.org/10.1016/j.mcat.2021.111486
30. A. E. Galashev, Russ. J. Phys. Chem. B **17**, 113–121 (2023). https://doi.org/10.1134/S1990793123010190
31. T. Wei, Y. Zhou, C. Sun, et al., Nano Res. **17**, 2763–2769 (2024). https://doi.org/10.1007/s12274-023-6187-8
32. U. Cardella, L. Decker, J. Sundberg, et al., Int. J. Hydrogen Energy **42**, 12339–12354 (2017). https://doi.org/10.1016/j.ijhydene.2017.03.167
33. A. Hammad and I. Dincer, Int. J. Hydrogen Energy **43**, 1139–1151 (2018). https://doi.org/10.1016/j.ijhydene.2017.10.158
34. O. A. Kim, T. V. Bogdan, A. E. Koklin, et al., Russ. J. Phys. Chem. B **16**, 1218–1220 (2022). https://doi.org/10.1134/S1990793122070107
35. M. A. Qyyum, Y. D. Chaniago, W. Ali, et al., Energies **13**, 5023 (2020). https://doi.org/10.3390/en13195023
36. A. H. Davtyan, Z. H. Manukyan, S. D. Arsentev, et al., Russ. J. Phys. Chem. B **18**, 461–467 (2024). https://doi.org/10.1134/S1990793124020209
37. X. Yu, X. Zhang, H. Wang, et al., J. Phys. Chem. C **121**, 22081–22091 (2017). https://doi.org/10.1021/acs.jpcc.7b06361
38. F. Mollaamin and M. Monajjemi, J. Mol. Model. **29**, 119 (2023). https://doi.org/10.1007/s00894-023-05526-3
39. E. Rivard, M. Trudeau, K. Zaghib, Materials **12**, 1973 (2019). https://doi.org/10.3390/ma12121973
40. F. Mollaamin and M. Monajjemi, Russ. J. Phys. Chem. B **17**, 658–672 (2023). https://doi.org/10.1134/S1990793123030223
41. F. Mollaamin and M. Monajjemi, Russ. J. Phys. Chem. B **18**, 607–623 (2024). https://doi.org/10.1134/S1990793124020271
42. F. Mollaamin, S. Shahriari, and Monajjemi, M. Russ. J. Phys. Chem. B **18**, 398–418 (2024). https://doi.org/10.1134/S199079312402026X
43. V. Y. Agroskin, B. G. Bravy, G. K.Vasiliev, et al., Russ. J. Phys. Chem. B **16**, 596–601 (2022). https://doi.org/10.1134/S1990793122040029
44. V. L. Chandraboss, B. Karthikeyana, and S. Senthilvelan, Phys. Chem. Chem. Phys. **17**, 12100–12114 (2015). https://doi.org/10.1039/C5CP00451A
45. Y. Xu, W. Fan, N. Chino, et al., Chem. Lett. **33**, 74–75 (2004). https://doi.org/10.1246/cl.2004.74
46. Y. Xu, W. Fan, S. P. Elangovan, et al., EurJIC **2004**, 4547–4549 (2004). https://doi.org/10.1002/ejic.200400566
47. Y. Liu, C.-P. Liu, C.-Y. Mang, et al., Spectrochim. Acta, Part A **283**, 121710 (2022). https://doi.org/10.1016/j.saa.2022.121710
48. A. E. Smygalina and A. D. Kiverin, Russ. J. Phys. Chem. B **17**, 907–914 (2023). https://doi.org/10.1134/S1990793123040188
49. F. Mollaamin and M.Monajjemi, Russ. J. Phys. Chem. B **18**, 533–548 (2024). https://doi.org/10.1134/S199079312402012X
50. B. Khalili Hadad, F. Mollaamin, and M. Monajjemi, Russ. Chem. Bull. **60**, 238–241 (2011). https://doi.org/10.1007/s11172-011-0039-5
51. F. Mollaamin, S. Mohammadi, Z. Khalaj, et al., Russ. J. Phys. Chem. B **18**, 67–82 (2024). https://doi.org/10.1134/S1990793124010330
52. M. Monajjemi, F. Mollaamin, and S. Shojaei, Biointerface Res. Appl. Chem. **10**, 5575 (2020). https://doi.org/10.33263/BRIAC103.575585
53. F. Mollaamin and M. Monajjemi, Comput. Theor. Chem. **1237**, 114666 (2024). https://doi.org/10.1016/j.comptc.2024.114666
54. S. Shahriari, F. Mollaamin, and M. Monajjemi, Micromachines **14**, 241 (2023). https://doi.org/10.3390/mi14020241
55. F. Mollaamin and M. Monajjemi, J. Mol. Struct. **1300**, 137214 (2024). https://doi.org/10.1016/j.molstruc.2023.137214
56. F. Mollaamin, A. Ilkhani, N. Sakhaei, et al., J. Comput. Theor. Nanosci. **12**, 3148–3154 (2015). https://doi.org/10.1166/jctn.2015.4092
57. F. Mollaamin and M. Monajjemi, Sens. Rev. **44**, 179–193 (2024). https://doi.org/10.1108/SR-01-2024-0066
58. M. Monajjemi, L. Mahdavian, F. Mollaamin, et al., Russ. J. Inorg. Chem. **54**, 1465–1473 (2009). https://doi.org/10.1134/S0036023609090216
59. F. Mollaamin and M. Monajjemi, Russ. J. Phys. Chem. B **18**, 49–66 (2024). https://doi.org/10.1134/S1990793124010159
60. F. Mollaamin and M. Monajjemi, Int. J. Quantum Chem. **124**, e27348 (2024). https://doi.org/10.1002/qua.27348
61. F. Mollaamin and M. Monajjemi, Mol. Simul. **49**, 365–376 (2023). https://doi.org/10.1080/08927022.2022.2159996
62. S. V. Feskov, Russ. J. Phys. Chem. B **18**, 1–8 (2024). https://doi.org/10.1134/S1990793124010081
63. M. J. Frisch, G. W. Trucks, H. B. Schlegel, G. E. Scuseria, M. A. Robb, J. R. Cheeseman, G. Scalmani, V. Barone, G. A. Petersson, H. Nakatsuji, X. Li, M. Caricato, A. V. Marenich, J. Bloino, B. G. Janesko, R. Gomperts, B. Mennucci, H. P. Hratchian, J. V. Or-

tiz, A. F. Izmaylov, J. L. Sonnenberg, D. Williams-Young, F. Ding, F. Lipparini, F. Egidi, J. Goings, B. Peng, A. Petrone, T. Henderson, D. Ranasinghe, V. G. Zakrzewski, J. Gao, N. Rega, G. Zheng, W. Liang, M. Hada, M. Ehara, K. Toyota, R. Fukuda, J. Hasegawa, M. Ishida, T. Nakajima, Y. Honda, O. Kitao, H. Nakai, T. Vreven, K. Throssell, J. A. Montgomery, Jr., J. E. Peralta, F. Ogliaro, M. J. Bearpark, J. J. Heyd, E. N. Brothers, K. N. Kudin, V. N. Staroverov, T. A. Keith, R. Kobayashi, J. Normand, K. Raghavachari, A. P. Rendell, J. C. Burant, S. S. Iyengar, J. Tomasi, M. Cossi, J. M. Millam, M. Klene, C. Adamo, R. Cammi, J. W. Ochterski, R. L. Martin, K. Morokuma, O. Farkas, J. B. Foresman, and D. J. Fox, *Gaussian 16, Revision C.01* (Gaussian, Inc., Wallingford CT, 2016).

64. R. Dennington, T. A. Keith, and J. M. Millam, *GaussView, Version 6.06.16* (Semichem Inc., Shawnee Mission, KS, 2016).
65. Z. Xu, C. Qin, Y. Yu, et al., AIP Adv. **14**, 055114 (2024). https://doi.org/10.1063/5.0208082
66. N. M. O'Boyle, A. L. Tenderholt, and K. M. Langner, J. Comput. Chem. **29**, 839–845 (2008). https://doi.org/10.1002/jcc.20823
67. C. F. Matta, P. W. Ayers, and R. Cook, "The physics of electron localization and delocalization," in *Electron Localization-Delocalization Matrices. Lecture Notes in Chemistry* (Springer, Cham, 2024), Vol. 112. https://doi.org/10.1007/978-3-031-51434-0_2
68. R. F. W. Bader, Theor. Chem. Accounts: Theory, Comput., Model. **105**, 276–283 (2001). https://doi.org/10.1007/s002140000233
69. T. Lu and F. Chen, J. Comput. Chem. **33**, 580–592 (2012). https://doi.org/10.1002/jcc.22885
70. A. D. Becke and K. E. Edgecombe, J. Chem. Phys. **92**, 5397–5403. (1990). https://doi.org/10.1063/1.458517
71. A. Savin, O. Jepsen, J. Flad, et al., Angew. Chem. Int. Ed. Engl. **31**, 187–188 (1992). https://doi.org/10.1002/anie.199201871
72. Z. Trontelj, J. Pirnat, V.Jazbinšek, et al., Crystals **10**, 450 (2020). . https://doi.org/10.3390/cryst10060450
73. F. Mollaamin, S. Shahriari, M. Monajjemi, et al., J. Cluster Sci. **34**, 1547–1562 (2023). https://doi.org/10.1007/s10876-022-02335-1
74. F. Mollaamin and M. Monajjemi, J. Mol. Model. **29**, 170 (2023). https://doi.org/10.1007/s00894-023-05567-8
75. F. Mollaamin, J. Comput. Theor. Nanosci. **11**, 2393–2398 (2014). https://doi.org/10.1166/jctn.2014.3653
76. L. G. Ekedahl, M. Eriksson, and I. Lundström, Acc. Chem. Res. **31**, 249–256 (1998). https://doi.org/10.1021/ar970068s
77. X. Li, J.-Y. Hwang, S. Shi, et al., Carbon **48**, 876–880 (2010). https://doi.org/10.1016/j.carbon.2009.10.042
78. K. Liu, E. Ko, S. Kim, et al., J. Phys. D: Appl. Phys. **52**, 155101 (2019). https://doi.org/10.1088/1361-6463/ab014e
79. E. V. Morozov, A. V. Il'ichev, and V. M. Bouznik, Russ. J. Phys. Chem. B **17**, 1361–1369 (2023). https://doi.org/10.1134/S1990793123060064
80. G. Conte, C. Simari, A.-M. Putz, et al., Int. J. Hydrogen Energy **48**, 27319–27329 (2023). https://doi.org/10.1016/j.ijhydene.2023.03.350